

Manipulating optical and electronic properties through interfacial ferroelectricity

Yulu Liu(刘钰璐), Gan Liu(刘敢), and Xiaoxiang Xi(奚啸翔)

Citation: Chin. Phys. B, 2025, 34 (**1**): 017701. DOI: 10.1088/1674-1056/ad9456

What follows is a list of articles you may be interested in

$BaTiO_3$/p-GaN/Au self-driven UV photodetector with bipolar photocurrent controlled by ferroelectric polarization

Wushuang Han(韩无双), Kewei Liu(刘可为), Jialin Yang(杨佳霖), Yongxue Zhu(朱勇学), Zhen Cheng(程祯), Xing Chen(陈星), Binghui Li(李炳辉), Lei Liu(刘雷), and Dezhen Shen(申德振)

Chin. Phys. B, 2024, 33 (**4**): 047701. DOI: 10.1088/1674-1056/ad2607

Charge trapping effect at the interface of ferroelectric/interlayer in the ferroelectric field effect transistor gate stack

Xiaoqing Sun(孙晓清), Hao Xu(徐昊), Junshuai Chai(柴俊帅), Xiaolei Wang(王晓磊), and Wenwu Wang(王文武)

Chin. Phys. B, 2023, 32 (**8**): 087701. DOI: 10.1088/1674-1056/acd524

Ferroelectricity induced by the absorption of water molecules on double helix SnIP

Dan Liu(刘聃), Ran Wei(魏冉), Lin Han(韩琳), Chen Zhu(朱琛), and Shuai Dong(董帅)

Chin. Phys. B, 2023, 32 (**3**): 037701. DOI: 10.1088/1674-1056/ac7f8e

Efficiently enhanced energy storage performance of $Ba_2Bi_4Ti_5O_{18}$ film by co-doping Fe^{3+} and Ta^{5+} ion with larger radius

Qiong Wu(吴琼), Lei Zhao(赵雷), Xinghao Chen(陈兴豪), and Shifeng Zhao(赵世峰)†

Chin. Phys. B, 2022, 31 (**9**): 097701. DOI: 10.1088/1674-1056/ac5393

Insight into influence of thermodynamic coefficients on transient negative capacitance in Zr-doped HfO_2 ferroelectric capacitors

Yuan-Yuan Zhang(张元元), Xiao-Qing Sun(孙晓清), Jun-Shuai Chai(柴俊帅), Hao Xu(徐昊), Xue-Li Ma(马雪丽), Jin-Juan Xiang(项金娟), Kai Han(韩锴), Xiao-Lei Wang(王晓磊), and Wen-Wu Wang(王文武)

Chin. Phys. B, 2021, 30 (**12**): 127701. DOI: 10.1088/1674-1056/ac01c4

TOPICAL REVIEW — Moiré physics in two-dimensional materials

Manipulating optical and electronic properties through interfacial ferroelectricity

Yulu Liu(刘钰璐)[1], Gan Liu(刘敢)[1], and Xiaoxiang Xi(奚啸翔)[1,2,3,†]

[1] *National Laboratory of Solid State Microstructures and Department of Physics, Nanjing University, Nanjing* 210093, *China*
[2] *Collaborative Innovation Center of Advanced Microstructures, Nanjing University, Nanjing* 210093, *China*
[3] *Jiangsu Physical Science Research Center, Nanjing* 210093, *China*

(Received 27 September 2024; revised manuscript received 2 November 2024; accepted manuscript online 19 November 2024)

Interfacial ferroelectricity is a recently established mechanism for generating spontaneous reversible electric polarization, arising from the charge transfer between stacked van der Waals layered atomic crystals. It has been realized in both naturally formed multilayer crystals and moiré superlattices. Owing to the large number of material choices and combinations, this approach is highly versatile, greatly expanding the scope of ultrathin ferroelectrics. A key advantage of interfacial ferroelectricity is its potential to couple with preexisting properties of the constituent layers, enabling their electrical manipulation through ferroelectric switching and paving the way for advanced device functionalities. This review article summarizes recent experimental progress in interfacial ferroelectricity, with an emphasis on its coupling with a variety of electronic properties. After introducing the underlying mechanism of interfacial ferroelectricity and the range of material systems discovered to date, we highlight selected examples showcasing ferroelectric control of excitonic optical properties, Berry curvature effects, and superconductivity. We also discuss the challenges and opportunities that await further studies in this field.

Keywords: interfacial ferroelectricity, sliding ferroelectricity, moiré ferroelectricity

PACS: 77.80.–e, 81.07.–b

DOI: 10.1088/1674-1056/ad9456 **CSTR:** 32038.14.CPB.ad9456

1. Introduction

Ferroelectricity is characterized by spontaneous electric polarization, which breaks inversion symmetry and can be switched by electric fields. Ferroelectric materials have diverse applications, including non-volatile memories, optoelectronics, transistors, energy harvesting and storage.[1,2] The study of the mechanisms, material realizations, and technical applications of ferroelectricity have been a vibrant interdisciplinary research field. Historically, ferroelectric materials were discovered in bulk crystals, in which the collective displacement of specific ions within the crystal lattice leads to the formation of electric dipoles and results in macroscopic polarization.[1,2] In contemporary studies of phase transitions in reduced dimensions and the development of functional devices, the quest to understand the thickness limit of ferroelectricity, alongside the growing demand for device miniaturization and low energy consumption, has driven the pursuit of ultrathin ferroelectrics. Although conventional ferroelectric materials can be grown as thin films using state of the art fabrication techniques, their performance often deteriorates at the two-dimensional (2D) limit due to depolarization effects.[3] Only in the last decade, high-quality crystalline ferroelectric thin films approaching the 2D limit have been synthesized, including SnTe,[4] $BiFeO_3$,[5] and doped HfO_2,[6] which surprisingly exhibit enhanced Curie temperature or electric polarization compared to their bulk counterparts.

Van der Waals layered materials offer a versatile platform to push ferroelectricity to the 2D limit. Some materials can possess the displacive-type ferroelectricity in the layer unit, such that when they are cast into the form of thin films the ferroelectric properties are largely preserved. Typical examples include $CuInP_2S_6$,[7] α-In_2Se_3,[8–10] and d1T-$MoTe_2$.[11] For certain elements without a definitive metallic or insulating character, their flexible bonding capability can induce coordinated charge transfer that gives rise to ferroelectricity even in a single-element monolayer, as demonstrated in black phosphorous-like bismuth.[12] However, such layered materials are rare, limiting the fundamental study of 2D ferroelectricity and their potential applications. In recent years, a new form of 2D ferroelectricity relying on interlayer interaction instead of intralayer ionic displacement has been theoretically proposed[13] and experimentally realized.[14–16] Broadly referred to as interfacial ferroelectricity, it includes both naturally occurring multilayer systems made of a single material and artificially assembled homo- or hetero-structures, the latter known as moiré ferroelectricity. With the vast range of van der Waals layered materials, interfacial ferroelectricity establishes a new paradigm for 2D ferroelectricity, opening up

†Corresponding author. E-mail: xxi@nju.edu.edu

© 2025 Chinese Physical Society and IOP Publishing Ltd. All rights, including for text and data mining, AI training, and similar technologies, are reserved.

opportunities for the rational design of material systems, the discovery and control of emergent physical properties, and the realization of advanced functional devices.

The field of interfacial ferroelectricity is evolving rapidly, and many excellent reviews are now available,[17–23] which provide comprehensive overview of this intriguing phenomenon. In light of these informative resources, in this brief review we will focus on one special aspect of interfacial ferroelectricity, namely, its coupling with other electronic properties. The emergence of interfacial ferroelectricity due to interlayer interactions suggests the potential for ferroelectric control over the preexisting properties of the constituent layers. This is because interlayer interaction is the primary cause of the dimensionality-dependent properties in van der Waals layered crystals. Among the various physical properties, we will focus on exciton optoelectronics, Berry curvature effects, and superconductivity, summarizing recent experimental advancements and offering our perspectives on the key challenges and opportunities in this field.

2. Mechanism and material realization of interfacial ferroelectricity

Interfacial ferroelectricity can be realized by stacking layered materials. The broken inversion symmetry of ferroelectricity sets constraints on both the choice of constituent layers and the stacking order. Guided by symmetry analysis, ferroelectricity can only be found in materials belonging to 10 polar point groups.[1] Such analysis on the stacking of the same monolayer material to form a ferroelectric bilayer has been thoroughly carried out, forming a general theory.[24] In practice, ferroelectricity also requires reversible electric polarization, and the electrical switching between different domain states must be realized through a specific pathway. Analogous to conventional ferroelectrics, this is typically achieved through electrically driven domain wall motion, which causes one domain type to expand at the expense of the other. However, unlike in conventional ferroelectrics, where an applied electric field drives the relocation of specific ions between energetically equivalent atomic sites, the electric field in this case induces the relative sliding of constituent layers to reverse the polarization, a mechanism referred to as sliding ferroelectricity.[13] Microscopically, the electric dipoles are induced by interlayer charge transfer, and the sliding by a fraction of lattice constant can alter the vertical atomic registry, reversing the direction of charge transfer and thereby switching the electric polarization.

This concept is illustrated in Fig. 1 using a simple bilayer hexagonal boron nitride (hBN). In the naturally grown hBN bulk crystal, the unit cell adopts the H-type stacking, in which the adjacent two layers are anti-parallel. This configuration, called AA′ in Fig. 1(a), is centrosymmetric, excluding ferroelectricity. However, in the R-type stacked configuration with the two layers in parallel, inversion symmetry can be broken. The two most stable configurations, AB and BA as illustrated in Figs. 1(b) and 1(c), correspond to the two polarization states and are connected by relative sliding between the layers. Because the interlayer interaction is of the van der Waals type, the energy cost for the sliding can be quite low, on the order of 10 meV/unit cell.[13] As a result, this process can be achieved with a manageable applied electric field. Interestingly, introducing a small twist angle between the R-stacked layers can induce a moiré pattern, which hosts both AB and BA configurations [Fig. 1(d)]. This leads to alternating domains with opposite polarizations on a moiré superlattice, a phenomenon known as moiré ferroelectricity.[13] Moiré ferroelectricity in hBN was observed experimentally in artificially stacked bilayer samples.[15,16] Although ferroelectricity does not exist in naturally grown hBN, it has recently been shown in the 3R phase of multilayer samples (referred to as rBN) grown using a specialized bevel-edge epitaxy technique.[25]

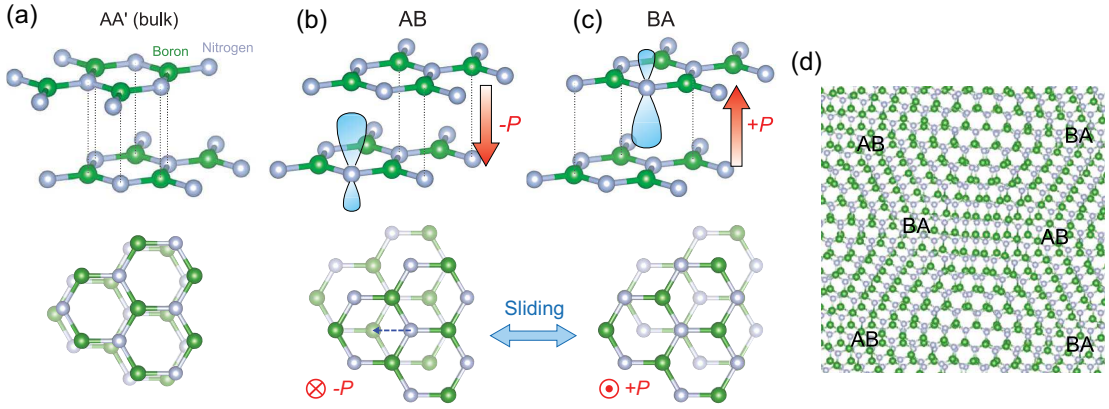


Fig. 1. (a) Stacking configuration for naturally grown hBN crystals with AA′ configuration. (b) and (c) Two stacking configurations for ferroelectric bilayer hBN. In panels (a)–(c), the first (second) row shows the cross-section (top) view. In the AB configuration (b), the boron atoms in the top layer and the nitrogen atoms in the bottom layer are vertically aligned. The charge transfer between them results in distortion of the boron p_z orbitals and creates a downward electric polarization. Lateral sliding by one boron-nitrogen bond length changes the AB configuration to the BA configuration (c), which reverses the vertical alignment of boron and nitrogen atoms in the two layers and results in an opposite polarization. (d) R-stacked bilayer hBN with a small twist angle, which generates a moiré superlattice hosting AB- and BA-stacked regions. The first (second) row figures in panels (a)–(c) are reproduced with permission from Ref. [15] (Ref. [26]).

Based on the principle discussed above, interfacial ferroelectricity can be generated starting from a monolayer crystal both in certain bilayer configurations directly extracted from the bulk crystal and in artificially stacked moiré bilayers. Typical examples of the former include 3R-MoS_2,[27–29] T_d-WTe_2,[14] T_d-$MoTe_2$,[30] and 1T′-ReS_2.[31] The latter includes twisted bilayer trigonal-prismatic transition metal dichalcogenides (TMDs), such as MoS_2, $MoSe_2$, WS_2, and WSe_2.[32,33] Since the ferroelectricity arises from interlayer interaction, this principle can be extended to multilayer systems with[34] or without[14,27,31,35] interlayer twist, and even to bulk crystals.[36] This extension enriches the possible domain structures with distinct polarization states and switching dynamics[27,34] and enhances the total polarization when the local dipoles at each interface add up coherently.[37] This principle is also not limited to bilayers or multilayers made of the same monolayer component. For example, heterobilayer of MoS_2/WS_2 grown by a one-step chemical vapor deposition process was also shown to host interfacial ferroelectricity, and no moiré effect is present in this case because the two layers are commensurate by growth.[38]

The heterostructure approach can be employed to broaden the scope of interfacial ferroelectricity due to the vast number of possible material combinations. However, the specific mechanism of charge transfer can be more complex than in homostructures. A typical example is the Bernal-stacked bilayer graphene aligned with top and bottom hBN encapsulation layers in a dual-gate device, in which unconventional ferroelectricity was reported.[39] The ferroelectricity is gate-specific, namely, only one of the gates can induce hysteretic change to the graphene resistance, whereas the other gate is anomalously screened over a wide range of applied bias. It was initially attributed to correlation-driven charge transfer between the two graphene layers, facilitated by the combined effects of the moiré pattern induced by the aligned hBN and an applied displacement field.[39] However, a later work found that the amount of charge transfer ($\sim 10^{13}$ cm^{-2}) exceeds the capacity of the moiré band,[40] challenging the original interpretation. The associated electric polarization (5 pC·m^{-1}) is among the highest in the reported interfacial ferroelectrics. Moreover, a recent preprint reported unconventional ferroelectricity even when bilayer graphene was replaced with monolayer graphene and when a lattice-mismatched WSe_2 layer was embedded between BN and graphene.[41] These observations suggest that the moiré effect may not play a central role. Instead, it has been proposed that the ferroelectricity originates from the specific BN. Although the mechanism of this unconventional ferroelectricity is still under debate, synaptic transistors with room-temperature neuromorphic functionality have been demonstrated using such a device.[42]

In the following section, we will focus on a few selected systems from those discussed above, in which the coupling between interfacial ferroelectricity and excitonic optical properties, Berry curvature effects or superconductivity has been experimentally demonstrated.

3. Coupling of interfacial ferroelectricity with other properties

3.1. Optoelectronic properties

The 2D semiconducting TMDs exhibit remarkable optical properties due to their large exciton binding energy and the presence of both spin and valley degrees of freedom.[43] Interfacial ferroelectricity has been found both in their few-layer 3R-stacked configuration[27–29] and in their moiré homobilayers.[32,33] With a small twist angle, these homobilayers undergo lattice reconstruction,[44] leading to AB- and BA-stacked domains hosting out-of-plane electric polarization. Currently, most studies focus on the visualization of the ferroelectric domains and characterization of the polarization switching dynamics. Since the two adjacent layers are asymmetrically coupled and the out-of-plane polarization induces a potential difference between them, the resulting band shift is expected to reshape the excitonic properties. As a result, ferroelectric control of excitonic properties can in principle be achieved using an external electric field in such systems.

A clear demonstration of this effect has been reported in bilayer 3R-MoS_2.[28] This system consists of two parallel-stacked MoS_2 monolayers with a lateral relative shift, which breaks the mirror symmetry with respect to the horizontal plane [Fig. 2(a)]. This results in two stable configurations, AB and BA, with top views resembling those of ferroelectric bilayer hBN as shown in Figs. 1(b) and 1(c). In the AB-stacked configuration, the Mo atoms in the top layer align vertically with the S atoms in the bottom layer, creating an upward electric polarization ($P > 0$) [Fig. 2(a)]; see also Ref. [37]. Density functional theory calculations reveal a type-II band alignment for this configuration,[45] with the conduction band wavefunction at the K point concentrated in the top layer while the valence band wavefunction at the Γ point equally distributed across both layers [Fig. 2(b), left]. This arises from the downward band shift of the top layer relative to the bottom layer, caused by the negative internal electric field associated with the positive ferroelectric polarization. As a result, the interlayer Γ–K indirect excitons exhibit a downward dipole moment $\boldsymbol{\mu}$.

These interlayer excitons appear as phonon replicas in photoluminesence (PL) spectra, along with their trion counterparts [Fig. 2(c)]. An external electric field $\boldsymbol{E}_{\rm ex}$ generated in a dual-gate device induces a Stark shift, $\Delta E = -\boldsymbol{E}_{\rm ex} \cdot \boldsymbol{\mu}$. The slope of this shift can be used to determine the direction of $\boldsymbol{\mu}$, with positive or negative values corresponding to $\boldsymbol{\mu}$ pointing downward or upward, respectively.[45,46] In the upper panel of Fig. 2(c), the external field range between -0.07 V/nm

and 0.08 V/nm shows a positive slope, corresponding to the AB-stacked configuration with $\boldsymbol{\mu}$ pointing down. Increasing the applied field counteracts the internal field and changes the band alignment above 0.08 V/nm, such that the direction of $\boldsymbol{\mu}$ is flipped, manifested as a sign change of the slope. Decreasing the field below −0.07 V/nm, past a coercive field E_c, switches the ferroelectric polarization to become negative, causing the exciton and trion peaks to abruptly blueshift because the internal field turns positive. The switching behavior is hysteretic, as shown in Fig. 2(c) for forward and backward sweeps. The intralayer momentum-direct excitons at the K point also respond to ferroelectric polarization switching, as detailed in the original study.[28] However, in a related study of multilayer 3R-MoS_2 using reflectance contrast spectroscopy,[47] only the intralayer excitons showed sensitivity to the ferroelectric order, while the interlayer excitons remained unaffected. Further investigation is required to clarify whether this discrepancy stems from differences between bilayer and multilayer systems or the measurement techniques (PL vs. reflectance contrast spectroscopy).

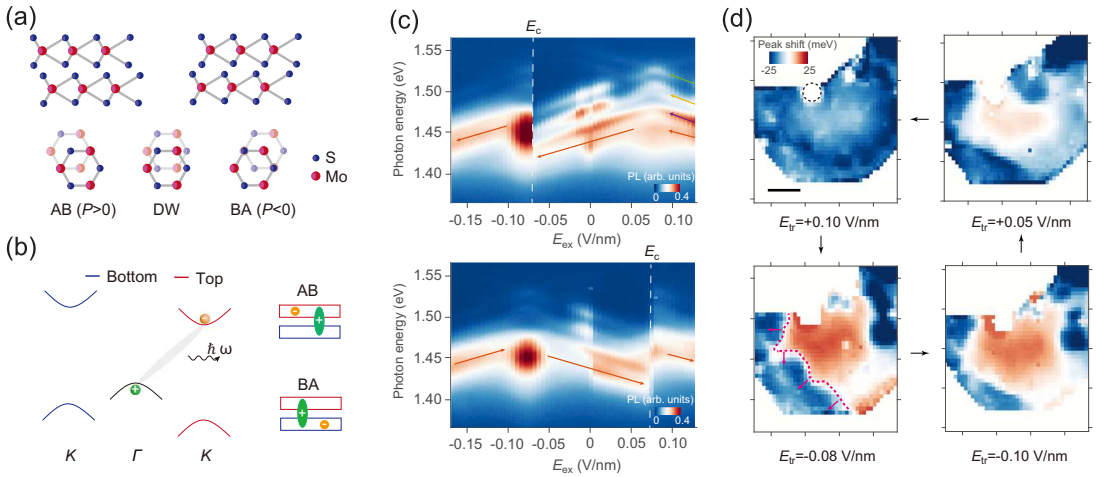


Fig. 2. (a) Bilayer 3R-MoS_2. The AB and BA configurations differ by a lateral relative shift between the two layers and have opposite polarization P. DW: domain wall. (b) Left: Effective type-II band alignment of bilayer AB-stacked 3R-MoS_2. Photoluminescence from momentum-indirect Γ–K excitons is illustrated. Right: The electron and hole distributions in the two layers for the AB- and BA-stacked configurations. External electric field is absent. (c) External electric field dependence of the PL spectra at 4 K, showing the Stark shift of the PL peaks and the sudden jump associated with polarization switching. The arrows indicate the direction of the field sweep. The four peaks are assigned to the phonon replicas of the Γ–K excitons and their trion counterparts. E_c: coercive field. (d) Real-space mapping of the Stark shift at different training fields E_{tr}. Blue and red colors correspond to AB- and BA-stacked domains, respectively. Figures reproduced with permission from Ref. [28].

The excitonic properties can in turn be used to visualize the ferroelectric domains based on far-field optical spectroscopy, providing valuable insight into the domain state switching process.[28] Figure 2(d) shows the evolution of the domain distribution as revealed by spatial-dependent Stark shift at different applied electric fields. The blue and red colors correspond to AB- and BA-stacked domains. The electrical switching of the domain state is realized through the movement of the domain wall. An important observation in this work is that the successful switching of ferroelectric domain state relies on the pre-existence of a domain wall, which can be induced during the mechanical exfoliation process, whereas switching in a single-domain sample proves to be challenging. This point was also noted in another work, which was attributed to strong pinning at the sample edge.[33] Domain walls are much more common in moiré homobilayers,[32,33] making the switching more accessible. These results raise the question of whether domain state switching in predicted interfacial ferroelectrics is always practically feasible.

The coupling of interfacial ferroelectricity with excitonic properties is expected to be common in a variety of systems, and its experimental realization awaits further exploration. So far few-layer 3R-MoS_2 is the only system in which ferroelectric modulation of excitonic properties has been reported. In semiconducting TMD moiré homobilayers, although Stark shift[45] and gate-tuned energy splitting of intralayer excitons[48] have been observed in PL measurements, and interfacial ferroelectricity has been established separately,[32,33] the coupling of these properties has not been discussed. In marginally twisted homobilayers, the size of the reconstructed domains can reach micron scale,[45] making far-field optical microspectroscopy still possible. To overcome the diffraction limit, it will be beneficial to develop techniques that integrate optical and scanning probes, such as near-field scanning optical spectroscopy.

3.2. Berry curvature effects

Berry curvature is a geometric property of electronic bands in momentum space, playing a crucial role in understanding various intriguing phenomena, such as the anomalous Hall effect and topological phases of matter.[49] In van der Waals layered topological materials, the interlayer interaction

can dramatically influence the electronic bands and the Berry curvature. Coupled with interfacial ferroelectricity, electrical switching of Berry curvature effects becomes possible.

WTe_2 is a prototypical material for demonstrating these properties. In its bulk form, it is a type-II topological Weyl semi-metal,[50,51] with nearly compensated electron and hole pockets at the Fermi surface leading to a large non-saturating magnetoresistance.[52] In the monolayer limit, it becomes a quantum spin Hall insulator, exhibiting edge conduction up to 100 K.[53] Electron doping through field-effect gating suppresses the insulating state in monolayer WTe_2 and induces superconductivity.[54,55] The manner in which the intrinsic insulating state is destroyed by charge carriers suggests an excitonic condensation mechanism for its origin.[56,57] However, first-principles calculations that neglect correlation effects also predict an insulating ground state driven by spin–orbit coupling.[58] As more layers are added, bilayer WTe_2 retains the insulating behavior, while trilayer and thicker samples become metallic, as indicated by the temperature dependence of electrical resistance.[14] Few-layer samples are noncentrosymmetric, enabling the observation of a nonlinear Hall effect as a manifestation of the Berry curvature dipole.[59,60] Because of time-reversal symmetry, the momentum-odd Berry curvature leads to a vanishing linear Hall effect, but the first-order moment of the Berry curvature can give rise to a second-order nonlinear Hall response, even in the absence of magnetic fields.[61] These results highlight the strong dependence of electronic, and particularly topological, properties on interlayer interactions in WTe_2.

Noncentrosymmetric few-layer WTe_2 is the first experimental system in which interfacial ferroelectricity was discovered.[14] In a dual-gate field-effect transistor with bilayer or trilayer WTe_2 as the channel, sweeping the electric field induces a butterfly-shaped dependence of the electrical conductance [Fig. 3(c)], characteristic of ferroelectric switching, which persists even above room temperature. This switching behavior is absent in monolayer samples, consistent with the ferroelectricity being an interfacial effect. The observation of ferroelectricity in the metallic trilayer WTe_2 is unusual, as itinerant electrons typically screen electrostatic force, making polar metals rare. However, this is possible in interfacial ferroelectricity, because the electric polarization is an interlayer effect and the conduction electrons are confined within the monolayer constituents, allowing them to coexist. Unlike bilayer 3R-MoS_2, which consists of noncentrosymmetric monolayers stacked in parallel [Fig. 2(a)], bilayer WTe_2 consists of centrosymmetric monolayers in the 1T′ coordination stacked in an anti-parallel configuration [Fig. 3(a)]. The two stable configurations are mirror symmetric about the central horizontal plane, and they exhibit opposite vertical polarizations due to uncompensated charge transfer.[63] This polarization can be switched by a slight sliding between the layers, as illustrated in Fig. 3(a). For samples thicker than bilayer, adjacent layers remain anti-parallel, and inversion symmetry is generally absent in the T_d-type stacking [Fig. 3(b)]. Ferroelectricity in these samples can similarly be explained by the sliding mechanism. The calculated vertical polarization of bilayer WTe_2, approximately 3.2×10^{11} e/cm^2, is consistent with the experimental value measured at 20 K.[63]

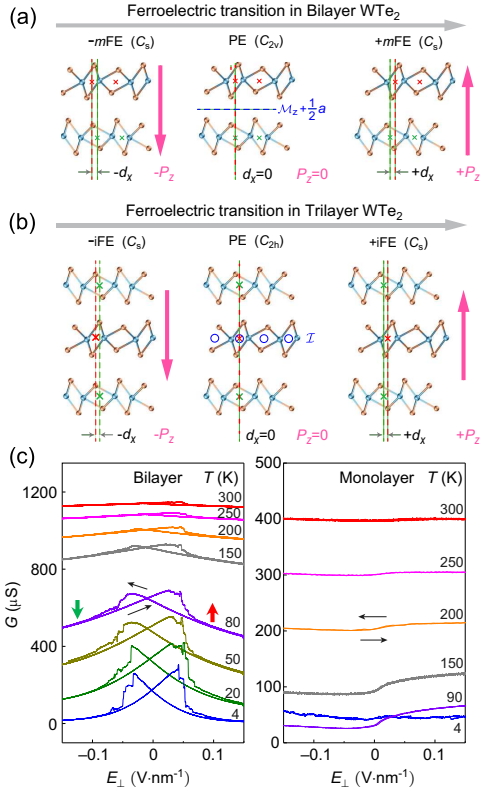


Fig. 3. (a) and (b) Schematic illustration of the ferroelectric switching pathways in bilayer and trilayer WTe_2. In bilayer WTe_2, the two ferroelectric states, denoted as $\pm m$FE, are related by a glide mirror operation, which consists of a reflection $\mathcal{M}_z$ about a horizontal mirror plane and an interlayer sliding. In trilayer WTe_2, the two ferroelectric states, denoted as $\pm$iFE, are related by an inversion operation $\mathcal{I}$. The intermediate paraelectric (PE) state for bilayer and trilayer WTe_2 exhibits C_{2v} and C_{2h} symmetry, respectively. (c) Conductance of bilayer and monolayer WTe_2 under a pure electric field generated in a dual-gate field effect transistor. Panels (a) and (b) are reproduced with permission from Ref. [62], and panel (c) is reproduced with permission from Ref. [14].

Ferroelectricity in multilayer WTe_2 is closely coupled with the Berry curvature at the Fermi level, offering a sensitive control of Berry curvature dipole.[35] In a dual-gate device, ferroelectric switching is observed in trilayer WTe_2 by tuning the vertical electric field, as reflected in the longitudinal electrical conductance [Fig. 4(a), upper panel]. The second-order Hall voltage $V_{\perp,2\omega}$ is dramatically modulated by the ferroelectric switching, exhibiting a sign change between the two polarization states [Fig. 4(a), lower panel]. This behavior correlates well with the calculated Berry curvature distribution in the Brillouin zone, which shows opposite Berry curvature dipoles for the two states [Fig. 4(b)]. Interestingly, while longitudinal conductance also shows ferroelectric switching for

tetralayer WTe_2, the corresponding nonlinear Hall voltage remains positive and follows a butterfly-shaped electric field dependence, without a sign reversal between the two polarization states.[35] This difference is explained by the distinct symmetry operations that relate the two polarization states in trilayer and tetralayer samples.[35,62] Specifically, for even-layer samples, the two polarization states are related by a glide mirror operation with respect to the *ab* plane ($\mathcal{M}_z$), while for odd-layer samples, they are related by an inversion operation ($\mathcal{I}$); see illustration in Figs. 3(a) and 3(b) for bilayer and trilayer WTe_2. Consequently, the out-of-plane Berry curvature pseudovector responds differently: $\mathcal{M}_z\Omega_z(k_x,k_y) = \Omega_z(k_x,k_y)$ for the even-layer case, whereas $\mathcal{I}_z\Omega_z(k_x,k_y) = \Omega_z(-k_x,-k_y) = -\Omega_z(k_x,k_y)$ for the odd-layer case. As a result, the Berry curvature dipole, defined as $D_{ij} = \int_k \Omega_j \partial_i f_0$, where Ω_j is the Berry curvature along the j direction and f_0 is the equilibrium electron distribution, undergoes a sign change during ferroelectric switching in odd-layer samples but does not change sign in even-layer samples. These findings demonstrate that multilayer WTe_2 offers a unique platform to achieve layer-parity-selective nonlinear Hall memory via non-volatile ferroelectric switching, which holds promise for advanced electronic applications.

The requirement of an odd number of layers for a sign-changing switch in the nonlinear Hall effect can be lifted by incorporating even-layer WTe_2 into a moiré superlattice.[64] By aligning the *a* axis of bilayer WTe_2 with the zigzag direction of monolayer WSe_2 in the trigonal prismatic coordination, a moiré superlattice with a rectangular unit cell is formed [Fig. 4(c)]. In this moiré system, WSe_2 remains charge neutral and the bilayer WTe_2 predominantly contributes to both the conduction and valence bands. The electric-field and filling-factor dependence of resistance exhibit peaks at filling factors of $\nu = 0, -1, -2$, which are attributed to the band insulating state of bilayer WTe_2, the correlated insulating state for the half-filled moiré band, and the band insulating state for the fully filled moiré band, respectively. The moiré-related insulating states are much stronger when the electric polarization in WTe_2 points away from WSe_2 ($P < 0$) [Fig. 4(d)], as the filled holes are driven to the upper monolayer of WTe_2 by the internal field, which experiences a stronger moiré potential at the WTe_2/WSe_2 interface. In this ferroelectric state, the redistribution of Berry curvature within the moiré Brillouin zone due to strong correlation effects leads to significant variations in the nonlinear Hall signal as the filling factor ν is varied [Fig. 4(e), upper panel and blue data in the lower panel]. In the opposite polarization state ($P > 0$), the moiré potential has a much weaker effect on charge transport, and the nonlinear Hall signal changes sign near $\nu = 0$ due to the reversal of the Berry curvature dipole at the edges of the conduction and valence bands [Fig. 4(e), middle panel and red data in the lower panel]. At a fixed filling factor with $-1 < \nu < 0$, switching the polarization state using an electric field can also induce a sign change in the nonlinear Hall signal [Fig. 4(e), upper and middle panels]. This work demonstrates the synergy between sliding ferroelectricity and moiré superlattice as an efficient approach to control Berry curvature effects and correlated electronic properties.

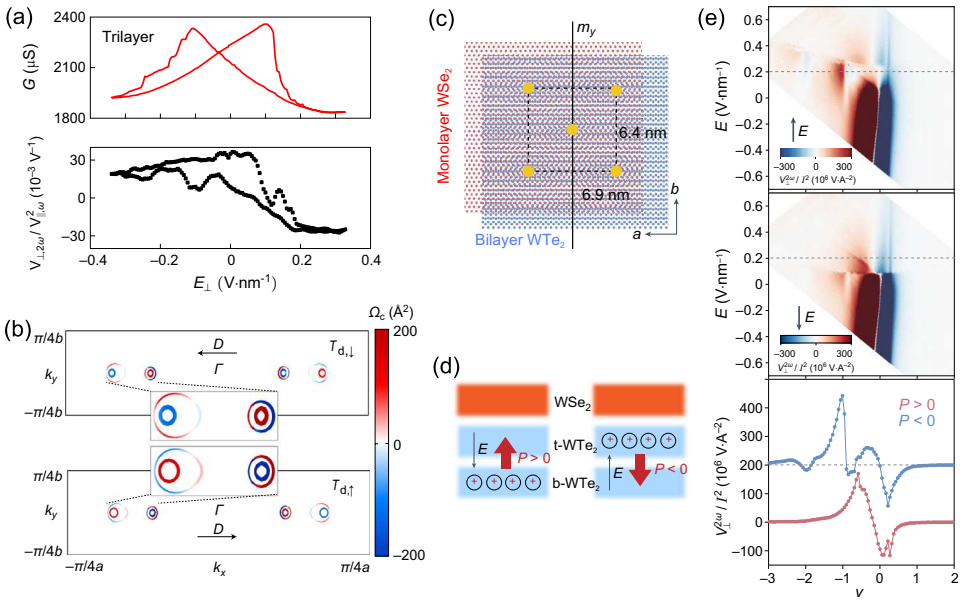


Fig. 4. (a) Electric-field-dependent longitudinal conductance (upper panel) and nonlinear Hall signal (lower panel) in trilayer WTe_2. (b) Calculated Berry curvature distribution in the Brillouin zone for trilayer WTe_2 shows opposite signs of the Berry curvature dipole D for the two ferroelectric states with opposite polarizations. (c) Moiré superlattice formed by monolayer WSe_2 and bilayer WTe_2, with only the W atoms shown for simplicity. The size of the rectangular moiré unit cell is labeled. (d) Polarization-controlled hole distribution in bilayer WTe_2. E is the corresponding internal electric field. (e) Top and central panels: The nonlinear Hall response as the external field and filling factor are varied. The arrows indicate the scan directions. Bottom panel: Data in the upper and central panels along the dashed lines. Panels (a) and (b) are reproduced with permission from Ref. [35], and panels (c)–(e) are reproduced with permission from Ref. [64].

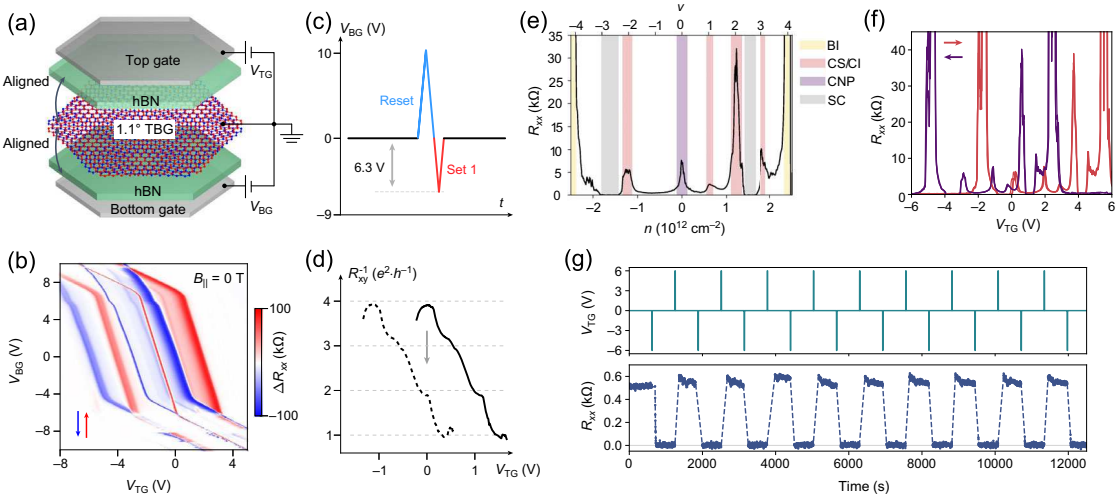


Fig. 5. (a) Schematic of a dual-gate device showing magic-angle twisted bilayer graphene aligned with top and bottom hBN gate dielectrics. (b) The resistance difference, ΔR_{xx}, as the back-gate voltage V_{BG} is swept forward and backward at different top-gate voltage V_{TG}. (c) The waveform of the V_{BG} pulse used for ferroelectrically resetting and setting the Chern insulating states. (d) Characterization of the Chern insulating state through the reciprocal transverse resistance, R_{xy}^{-1}, measured before (solid line) and after (dashed line) applying a V_{BG} pulse. (e) In another device with the same structure, the bottom gate tunes the longitudinal resistance R_{xx} as a function of carrier density (bottom axis) and the filling factor of the moiré unit cell (upper axis) at 40 mK, revealing band insulating states (BI), correlated semimetallic or insulating states (CS/CI), the charge neutrality point (CNP), and the superconducting state (SC). (f) The top-gate voltage induces a hysteretic response of R_{xx}, with arrows denoting voltage sweep directions. (g) V_{TG} pulses of ±6 V switch the system between the normal and superconducting states. Panels (a)–(d) are reproduced with permission from Ref. [65], and panels (e)–(g) are reproduced with permission from Ref. [73].

Interfacial ferroelectricity can also be used to switch topological edge states, as demonstrated in magic-angle twisted bilayer graphene (MATBG) aligned with hBN encapsulation layers.[65] A device schematic is shown in Fig. 5(a), where MATBG is aligned with both the top and bottom hBN layers, which also serve as gate dielectrics. This is similar to Bernal-stacked bilayer graphene aligned with hBN,[39,40] discussed in Section 2, and both systems exhibit unconventional ferroelectricity. MATBG hosts correlated flat bands with nontrivial topology,[66–72] and the coupling of these properties with ferroelectricity enables control of topological states. In this work,[65] gate-specific ferroelectricity was observed for the bottom gate, leading to hysteretic changes in the longitudinal resistance during forward and backward sweeps of V_{BG} [Fig. 5(b)]. This bottom gate is used to target specific Chern insulating states under an out-of-plane magnetic field, using the pulse waveform shown in Fig. 5(c). The pulse with a fixed positive amplitude resets the system into a fully polarized state, followed by a pulse with a variable negative amplitude which selectively sets the system into a particular Chern insulating state. The top gate does not induce ferroelectric switching but can be used for fine-tuning between Chern insulating states with distinct Chern numbers, as characterized by plateaus in the reciprocal Hall resistance from edge-state conduction [Fig. 5(d)]. Partial filling of the moiré Chern bands in MATBG leads to over a thousand ferroelectric states with quasi-continuous resistance levels, which can be deterministically addressed by V_{BG}, offering potential applications in topological neuromorphic computing.

The coupling of sliding ferroelectricity and Berry curvature effects is not limited to multilayer WTe_2 and MATBG/hBN heterostructures. For instance, ferroelectric topological insulators have been theoretically proposed in multilayer Bi_2Te_3,[74] exhibiting both in-plane and out-of-plane ferroelectricity in 2D topological insulators through specific interlayer sliding. Recently, the topological nontrivial bands in semiconducting TMD R-stacked moiré homobilayers, particularly the quantum anomalous Hall effect and fractional quantum anomalous Hall effect in twisted homobilayers of $MoTe_2$ and WSe_2, have garnered significant attention.[75–80] The roles of interfacial ferroelectricity and intralayer piezoelectricity have been recognized as key factors in determining the Chern numbers.[81] These developments suggest ferroelectric control of topological properties and topological phase transitions in these systems.

3.3. Superconductivity

Ferroelectric switching of superconductivity represents a new paradigm for the electrical control of superconductivity, characterized by bistable, nonvolatile behavior and holding promise for new superconducting electronic functionalities. This approach is distinct from the conventional methods of electrical tuning of superconductivity,[82] which typically rely on carrier doping to modify electronic properties, such as electron–phonon coupling or electron correlation, and therefore require continuous application of an external electric field. In systems similar to those discussed in Subsection 3.2, ferroelectric switching of superconductivity has been observed.[30,73]

MATBG is well known for its rich correlated electronic phases and superconductivity.[83,84] When aligned

with hBN layers, the emergent interfacial unconventional ferroelectricity[39,40] enables bistable switching of these properties. Similar to the device used for ferroelectric switching of topological edges states [Figs. 5(a)–5(d)], gate-specific ferroelectricity was also observed in another device.[73] In this device, the bottom gate tunes the filling of the moiré band, producing resistance peaks corresponding to the charge neutrality point, band insulating state, and correlated semimetallic/insulating states [Fig. 5(e)]. Superconductivity emerges on both electron- and hole-doping sides near half filling ($\nu = \pm 2$). The top gate voltage induces the same set of electronic phases, but the forward and backward voltage sweeps exhibit a hysteretic response, characteristic of ferroelectric switching [Fig. 5(f)]. By setting V_{BG} to achieve the hole-doped superconducting regime, V_{TG} pulses of ± 6 V can achieve highly reproducible switching between the normal and superconducting states [Fig. 5(g)]. This is due to the hysteretic modulation of the carrier density induced by the ferroelectric gate.

Ferroelectric switching of superconductivity has also been reported in bilayer T_d-$MoTe_2$[30] using a dual-gate device [Fig. 6(a)]. Because bilayer T_d-$MoTe_2$ is isostructural to bilayer WTe_2 [Fig. 3(a)], sliding ferroelectricity is naturally expected. Unlike the insulating temperature dependence of resistance in bilayer WTe_2,[14] bilayer T_d-$MoTe_2$ exhibits metallic behavior and superconducts at around 2 K.[30,85] As presented in Fig. 6(b), the normal state shows hysteretic switching in the sample resistance when sweeping the displacement field in opposite directions — a key signature for ferroelectricity. At even lower temperatures, the hysteretic response persists, showing switching between the superconducting and normal states. A typical set of data at 1.7 K is presented in Fig. 6(c). The sample starts from a normal state at high displacement field magnitudes and gradually transitions into the superconducting state. A sudden, first-order transition back to the normal state occurs when the displacement field reverses the electric polarization, indicating strong coupling between ferroelectricity and superconductivity. The temperature-dependent sweeps in Fig. 6(b) show that the maximum superconducting critical temperature is reached just before the superconducting state is destroyed by ferroelectric switching, suggesting a close relationship between superconductivity and the internal electric field in the sample. Note that in these switching behaviors, only the displacement field is varied, whereas the carrier density remains fixed. Figure 6(d) further demonstrates the reversibility of this switching process.

Although the superconductivity in MATBG and T_d-$MoTe_2$ can have different origins, their ferroelectric switching exhibits many common features. The switched state, whether superconducting or normal, persists until the next pulse arrives, demonstrating non-volatility [Figs. 5(g) and 6(d)]. The required displacement fields are both on the order of 1 V/nm. In both systems, the mechanism underlying the coupling between ferroelectricity and superconductivity is not yet fully understood, and the clarification of the origin of interfacial ferroelectricity is the first step. While the mechanism of ferroelectricity in MATBG aligned with hBN remains unsettled, the ferroelectricity in T_d-$MoTe_2$ is attributed to interlayer sliding.[30] Future experimental and theoretical studies are needed to unravel how the internal electric field generated by the ferroelectric polarization impacts the electronic band structure and consequently the superconductivity.

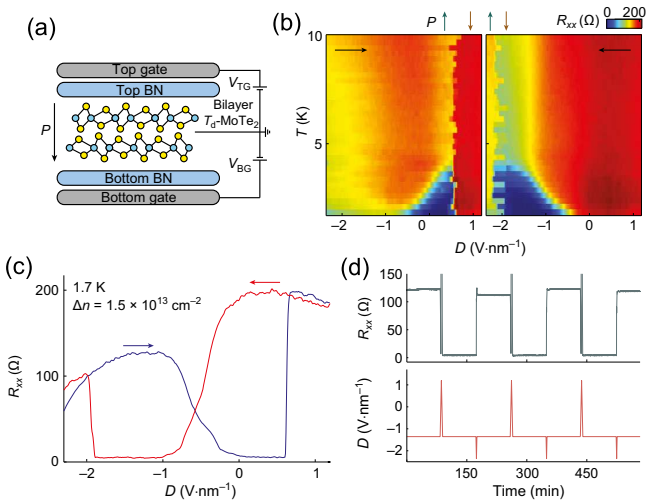


Fig. 6. (a) Dual-gate device structure for bilayer T_d-$MoTe_2$. (b) Temperature and displacement field dependence of the longitudinal resistance. The arrows on the top denote the internal polarization directions. (c) A horizontal cut of the data in (b) at 1.7 K showing the switching between bistable normal and superconducting states. Horizontal arrows in panels (b) and (c) represent the sweep directions of the displacement field. (d) Reversible switching between superconducting and normal states using pulses of displacement field. All data are for a fixed electron doping of 1.5×10^{13} cm^{-2}. Figures reproduced with permission from Ref. [30].

Theoretically, the coexistence of ferroelectricity and superconductivity has been predicted in $CuNb_2Se_4$, a bilayer 2H-$NbSe_2$ intercalated by Cu.[86] It was proposed that ferroelectric switching could flip the sign of spin–orbit coupling-induced spin splitting and reverse the superconducting diode effect. Although the ferroelectricity in $CuNb_2Se_4$ is not interfacial in nature, the proposed effect may be applicable to interfacial ferroelectricity as well. Experimentally, 3R-$NbSe_2$ has recently been synthesized,[87] and it is expected to host superconductivity because its monolayer constituent superconducts.[88] Because 3R-$NbSe_2$ is isostructural to 3R-MoS_2,[27–29] sliding ferroelectricity may also exist in this system. However, $NbSe_2$ has a sheet carrier density of approximately 10^{15} cm^{-2},[89] which is 2–3 orders of magnitude higher than that in T_d-$MoTe_2$ and MATBG,[30,73] leading to enhanced screening effects. These metallic systems present an intriguing opportunity to investigate whether an upper limit on carrier density exists for the realization of interfacial ferroelectricity and the ferroelectric switching of superconductivity.

4. Summary and outlook

We have discussed selected experimental works that demonstrate the coupling between interfacial ferroelectricity and various electronic properties. Specifically, mechanically exfoliated bilayer 3R-MoS_2, T_d-WTe_2, and T_d-$MoTe_2$ exhibit sliding ferroelectricity, which can be used to electrically modulate excitonic optical properties, the nonlinear Hall effect, and superconductivity, respectively. In WTe_2/WSe_2 and hBN/MATBG/hBN moiré systems, the moiré potential coupled with interfacial ferroelectricity not only induces a variety of electronic phases, such as correlated insulating states, Chern insulating states, and superconductivity, but also enables electrical manipulation of or even bistable switching between these states. Electrical control of many other properties is possible in interfacial ferroelectrics if they already exist in the constituent layers or emerge from stacking. For instance, stacking magnetic layered materials may induce ferroelectricity, as proposed in stacked CrI_3,[24] opening new avenues for engineering multiferroicity.[13,90–93] Inspired by the ferroelectric control of spin polarization in $BaTiO_3$-based tunnel junctions,[94] interfacial ferroelectricity may be utilized to control the spin splitting of electronic bands for spintronic applications.[95,96]

Although interfacial ferroelectricity provides an efficient means to manipulate the properties of two-dimensional materials, there are still many limitations and challenges. One major challenge is to extend the material realization of interfacial ferroelectricity to a broader range of systems. For interfacial ferroelectricity not involving a moiré superlattice, while many candidate materials have been predicted,[23] some may be thermodynamically unstable in the stacking configurations required for ferroelectricity. For example, many TMDs are stable only in the H-stacked non-ferroelectric phase, rather than the R-stacked ferroelectric phase. The prediction and synthesis of stable, high-quality crystals capable of hosting sliding ferroelectricity remain a challenge for both theorists and experimentalists. In the case of moiré ferroelectricity, although both homostructures and heterostructures have demonstrated interfacial ferroelectricity, the number of known examples is limited given the diversity of 2D materials. Theoretical guidance will be invaluable in efficiently identifying candidate systems, which must consider both symmetry requirements and material-specific parameters. For example, the work-function mismatch in heterostructures is a significant source of interlayer charge transfer, which may interfere with interfacial ferroelectricity.

Another challenge is the precise probing and control of ferroelectric domains. So far, most studies exploiting interfacial ferroelectricity to control other electronic properties, including some discussed in this article, have relied on macroscopic experimental probes, such as electrical transport. Due to inevitable domain distribution, the observed properties represent an average over different domains, which may differ from those of a single domain. Therefore, the visualization, investigation, and manipulation of ferroelectric domains at the relevant scale are essential. In interfacial ferroelectrics without moiré superlattices, the domain size can in principle be macroscopic, but sample inhomogeneities and defects may lead to domain distribution and domain-wall pinning. In moiré ferroelectricity, the domain distribution is even more complex due to lattice reconstruction. For fundamental studies of the coupling between interfacial ferroelectricity and other properties, microscopic probes are expected to offer deeper insights into the underlying mechanisms. These tools need to be integrated with the capability to electrically switch the ferroelectric order. In conventional ferroelectrics, domain walls can exhibit unique properties and offer additional functionalities.[97] In the same vein, domain walls in interfacial ferroelectricity may warrant investigation. From the perspective of applications, domain wall pinning can lead to variations in device performance, making it important to explore strategies that minimize this effect.

With its flexibility in material realization and the capability of electrical manipulation of diverse electronic properties, we believe that interfacial ferroelectricity holds great promise as a versatile platform for both uncovering new physical phenomena and driving advanced device applications.

Acknowledgments

Project supported by the Natural Science Foundation of Jiangsu Province (Grant Nos. BK20231529 and BK20233001), the National Key Research and Development Program of China (Grant No. 2024YFA1409100), the Fundamental Research Funds for the Central Universities (Grant No. 0204-14380233), the National Natural Science Foundation of China (Grant Nos. 12474170 and 123B2059), and the National Postdoctoral Program for Innovative Talents (Grant No. BX20240160).

References

[1] Wadhawan V 2000 *Introduction to Ferroic Materials*, 1st Edn. (CRC Press)
[2] Rabe K M, Ahn C H and Triscone J M (eds) 2007 *Physics of Ferroelectrics: A Modern Perspective* (Berlin, Heidelberg: Springer Berlin Heidelberg)
[3] Dawber M, Rabe K M and Scott J F 2005 *Rev. Mod. Phys.* **77** 1083
[4] Chang K, Liu J, Lin H, Wang N, Zhao K, Zhang A, Jin F, Zhong Y, Hu X, Duan W, Zhang Q, Fu L, Xue Q K, Chen X and Ji S H 2016 *Science* **353** 274
[5] Ji D, Cai S, Paudel T R, Sun H, Zhang C, Han L, Wei Y, Zang Y, Gu M, Zhang Y, Gao W, Huyan H, Guo W, Wu D, Gu Z, Tsymbal E Y, Wang P, Nie Y and Pan X 2019 *Nature* **570** 87
[6] Cheema S S, Kwon D, Shanker N, dos Reis R, Hsu S L, Xiao J, Zhang H, Wagner R, Datar A, McCarter M R, Serrao C R, Yadav A K, Karbasian G, Hsu C H, Tan A J, Wang L C, Thakare V, Zhang X, Mehta A, Karapetrova E, Chopdekar R V, Shafer P, Arenholz E, Hu C, Proksch R, Ramesh R, Ciston J and Salahuddin S 2020 *Nature* **580** 478

[7] Liu F, You L, Seyler K L, Li X, Yu P, Lin J, Wang X, Zhou J, Wang H, He H, Pantelides S T, Zhou W, Sharma P, Xu X, Ajayan P M, Wang J and Liu Z 2016 *Nat. Commun.* **7** 12357

[8] Zhou Y, Wu D, Zhu Y, Cho Y, He Q, Yang X, Herrera K, Chu Z, Han Y, Downer M C, Peng H and Lai K 2017 *Nano Lett.* **17** 5508

[9] Cui C, Hu W J, Yan X, Addiego C, Gao W, Wang Y, Wang Z, Li L, Cheng Y, Li P, Zhang X, Alshareef H N, Wu T, Zhu W, Pan X and Li L J 2018 *Nano Lett.* **18** 1253

[10] Xiao J, Zhu H, Wang Y, Feng W, Hu Y, Dasgupta A, Han Y, Wang Y, Muller D A, Martin L W, Hu P and Zhang X 2018 *Phys. Rev. Lett.* **120** 227601

[11] Yuan S, Luo X, Chan H L, Xiao C, Dai Y, Xie M and Hao J 2019 *Nat. Commun.* **10** 1775

[12] Gou J, Bai H, Zhang X, Huang Y L, Duan S, Ariando A, Yang S A, Chen L, Lu Y and Wee A T S 2023 *Nature* **617** 67

[13] Li L and Wu M 2017 *ACS Nano* **11** 6382

[14] Fei Z, Zhao W, Palomaki T A, Sun B, Miller M K, Zhao Z, Yan J, Xu X and Cobden D H 2018 *Nature* **560** 336

[15] Yasuda K, Wang X R, Watanabe K, Taniguchi T and Jarillo-Herrero P 2021 *Science* **372** 1458

[16] Stern M V, Waschitz Y, Cao W, Nevo I, Watanabe K, Taniguchi T, Sela E, Urbakh M, Hod O and Ben Shalom M 2021 *Science* **372** 1462

[17] Guan Z, Hu H, Shen X, Xiang P, Zhong N, Chu J and Duan C 2020 *Adv. Electron. Mater.* **6** 1900818

[18] Wu M H and Li J 2022 *Proc. Natl. Acad. Sci. USA* **118** e2115703118

[19] Zhang D, Schoenherr P, Sharma P and Seidel J 2023 *Nat. Rev. Mater.* **8** 25

[20] Zhang X and Peng B 2023 *J. Semicond.* **44** 011002

[21] Fan Z, Qu J, Wang T, Wen Y, An Z, Jiang Q, Xue W, Zhou P and Xu X 2023 *Chin. Phys. B* **32** 128508

[22] Chen J, Cui P and Zhang Z 2024 *Adv. Funct. Mater.* **34** 2408625

[23] Li S, Wang F, Wang Y, Yang J, Wang X, Zhan X, He J and Wang Z 2024 *Adv. Mater.* **36** 2301472

[24] Ji J, Yu G, Xu C and Xiang H J 2023 *Phys. Rev. Lett.* **130** 146801

[25] Wang L, Qi J, Wei W, Wu M, Zhang Z, Li X, Sun H, Guo Q, Cao M, Wang Q, Zhao C, Sheng Y, Liu Z, Liu C, Wu M, Xu Z, Wang W, Hong H, Gao P, Wu M, Wang Z J, Xu X, Wang E, Ding F, Zheng X, Liu K and Bai X 2024 *Nature* **629** 74

[26] Yasuda K, Zalys-Geller E, Wang X, Bennett D, Cheema S S, Watanabe K, Taniguchi T, Kaxiras E, Jarillo-Herrero P and Ashoori R 2024 *Science* **385** 53

[27] Meng P, Wu Y Z, Bian R J, Pan E, Dong B, Zhao X X, Chen J G, Wu L S, Sun Y Q, Fu Q D, Liu Q, Shi D, Zhang Q, Zhang Y W, Liu Z and Liu F C 2022 *Nat. Commun.* **13** 7696

[28] Yang D, Liang J, Wu J, Xiao Y, Dadap J I, Watanabe K, Taniguchi T and Ye Z 2024 *Nat. Commun.* **15** 1389

[29] Bian R, He R, Pan E, Li Z, Cao G, Meng P, Chen J, Liu Q, Zhong Z, Li W and Liu F 2024 *Science* **385** 57

[30] Jindal A, Saha A, Li Z Z, Taniguchi T, Watanabe K, Hone J C, Birol T, Fernandes R M, Dean C R, Pasupathy A N and Rhodes D A 2023 *Nature* **613** 48

[31] Wan Y, Hu T, Mao X, Fu J, Yuan K, Song Y, Gan X, Xu X, Xue M, Cheng X, Huang C, Yang J, Dai L, Zeng H and Kan E 2022 *Phys. Rev. Lett.* **128** 067601

[32] Wang X R, Yasuda K, Zhang Y, Liu S, Watanabe K, Taniguchi T, Hone J, Fu L and Jarillo-Herrero P 2022 *Nat. Nanotechnol.* **17** 367

[33] Weston A, Castanon E G, Enaldiev V, Ferreira F, Bhattacharjee S, Xu S G, Corte-León H, Wu Z F, Clark N, Summerfield A, Hashimoto T, Gao Y Z, Wang W D, Hamer M, Read H, Fumagalli L, Kretinin A V, Haigh S J, Kazakova O, Geim A K, Fal'ko V I and Gorbachev R 2022 *Nat. Nanotechnol.* **17** 390

[34] Van Winkle M, Dowlatshahi N, Khaloo N, Iyer M, Craig I M, Dhall R, Taniguchi T, Watanabe K and Bediako D K 2024 *Nat. Nanotechnol.* **19** 751

[35] Xiao J, Wang Y, Wang H, Pemmaraju C D, Wang S, Muscher P, Sie E J, Nyby C M, Devereaux T P, Qian X, Zhang X and Lindenberg A M 2020 *Nat. Phys.* **16** 1028

[36] Sharma P, Xiang F X, Shao D F, Zhang D, Tsymbal E Y, Hamilton A R and Seidel J 2019 *Sci. Adv.* **5** eaax5080

[37] Deb S, Cao W, Raab N, Watanabe K, Taniguchi T, Goldstein M, Kronik L, Urbakh M, Hod O and Ben Shalom M 2022 *Nature* **612** 465

[38] Rogée L, Wang L, Zhang Y, Cai S H, Wang P, Chhowalla M, Ji W and Lau S P 2022 *Science* **376** 973

[39] Zheng Z R, Ma Q, Bi Z, de la Barrera S, Liu M H, Mao N N, Zhang Y, Kiper N, Watanabe K, Taniguchi T, Kong J, Tisdale W A, Ashoori R, Gedik N, Fu L, Xu S Y and Jarillo-Herrero P 2020 *Nature* **588** 71

[40] Niu R R, Li Z X, Han X Y, Qu Z Z, Ding D D, Wang Z Y, Liu Q L, Liu T Y, Han C R, Watanabe K, Taniguchi T, Wu M H, Ren Q, Wang X Y, Hong J W, Mao J H, Han Z, Liu K H, Gan Z Z and Lu J M 2022 *Nat. Commun.* **13** 6241

[41] Niu R, Li Z, Han X, Liu Q, Qu Z, Wang Z, Han C, Watanabe K, Taniguchi T, Liu K, Mao J, Shi W, Peng B, Han Z V, Gan Z and Lu J 2024 arXiv:2403.17326 [cond-mat.mtrl-sci]

[42] Yan X, Zheng Z, Sangwan V K, Qian J H, Wang X, Liu S E, Watanabe K, Taniguchi T, Xu S Y, Jarillo-Herrero P, Ma Q and Hersam M C 2023 *Nature* **624** 551

[43] Mak K F and Shan J 2016 *Nat. Photon.* **10** 216

[44] Weston A, Zou Y, Enaldiev V, Summerfield A, Clark N, Zólyomi V, Graham A, Yelgel C, Magorrian S, Zhou M, Zultak J, Hopkinson D, Barinov A, Bointon T H, Kretinin A, Wilson N R, Beton P H, Fal'ko V I, Haigh S J and Gorbachev R 2020 *Nat. Nanotechnol.* **15** 592

[45] Sung J, Zhou Y, Scuri G, Zólyomi V, Andersen T I, Yoo H, Wild D S, Joe A Y, Gelly R J, Heo H, Magorrian S J, Bérubé D, Valdivia A M M, Taniguchi T, Watanabe K, Lukin M D, Kim P, Fal'ko V I and Park H 2020 *Nat. Nanotechnol.* **15** 750

[46] Ciarrocchi A, Unuchek D, Avsar A, Watanabe K, Taniguchi T and Kis A 2019 *Nat. Photon.* **13** 131

[47] Deb S, Krause J, Faria Junior P E, Kempf M A, Schwartz R, Watanabe K, Taniguchi T, Fabian J and Korn T 2024 *Nat. Commun.* **15** 7595

[48] Andersen T I, Scuri G, Sushko A, De Greve K, Sung J, Zhou Y, Wild D S, Gelly R J, Heo H, Bérubé D, Joe A Y, Jauregui L A, Watanabe K, Taniguchi T, Kim P, Park H and Lukin M D 2021 *Nat. Mater.* **20** 480

[49] Xiao D, Chang M C and Niu Q 2010 *Rev. Mod. Phys.* **82** 1959

[50] Soluyanov A A, Gresch D, Wang Z, Wu Q, Troyer M, Dai X and Bernevig B A 2015 *Nature* **527** 495

[51] Li P, Wen Y, He X, Zhang Q, Xia C, Yu Z M, Yang S A, Zhu Z, Alshareef H N and Zhang X X 2017 *Nat. Commun.* **8** 2150

[52] Ali M N, Xiong J, Flynn S, Tao J, Gibson Q D, Schoop L M, Liang T, Haldolaarachchige N, Hirschberger M, Ong N P and Cava R J 2014 *Nature* **514** 205

[53] Wu S, Fatemi V, Gibson Q D, Watanabe K, Taniguchi T, Cava R J and Jarillo-Herrero P 2018 *Science* **359** 76

[54] Fatemi V, Wu S, Cao Y, Bretheau L, Gibson Q D, Watanabe K, Taniguchi T, Cava R J and Jarillo-Herrero P 2018 *Science* **362** 926

[55] Sajadi E, Palomaki T, Fei Z, Zhao W, Bement P, Olsen C, Luescher S, Xu X, Folk J A and Cobden D H 2018 *Science* **362** 922

[56] Jia Y, Wang P, Chiu C L, Song Z, Yu G, Jack B, Lei S, Klemenz S, Cevallos F A, Onyszczak M, Fishchenko N, Liu X, Farahi G, Xie F, Xu Y, Watanabe K, Taniguchi T, Bernevig B A, Cava R J, Schoop L M, Yazdani A and Wu S 2022 *Nat. Phys.* **18** 87

[57] Sun B, Zhao W, Palomaki T, Fei Z, Runburg E, Malinowski P, Huang X, Cenker J, Cui Y T, Chu J H, Xu X, Ataei S S, Varsano D, Palummo M, Molinari E, Rontani M and Cobden D H 2022 *Nat. Phys.* **18** 94

[58] Qian X, Liu J, Fu L and Li J 2014 *Science* **346** 1344

[59] Ma Q, Xu S Y, Shen H, MacNeill D, Fatemi V, Chang T R, Mier Valdivia A M, Wu S, Du Z, Hsu C H, Fang S, Gibson Q D, Watanabe K, Taniguchi T, Cava R J, Kaxiras E, Lu H Z, Lin H, Fu L, Gedik N and Jarillo-Herrero P 2019 *Nature* **565** 337

[60] Kang K, Li T, Sohn E, Shan J and Mak K F 2019 *Nat. Mater.* **18** 324

[61] Sodemann I and Fu L 2015 *Phys. Rev. Lett.* **115** 216806

[62] Wang H and Qian X 2019 *npj Comput. Mater.* **5** 119

[63] Yang Q, Wu M and Li J 2018 *J. Phys. Chem. Lett.* **9** 7160

[64] Kang K, Zhao W, Zeng Y, Watanabe K, Taniguchi T, Shan J and Mak K F 2023 *Nat. Nanotechnol.* **18** 861

[65] Chen M, Xie Y, Cheng B, Yang Z, Li X Z, Chen F, Li Q, Xie J, Watanabe K, Taniguchi T, He W Y, Wu M, Liang S J and Miao F 2024 *Nat. Nanotechnol.* **19** 962

[66] Nuckolls K P, Oh M, Wong D, Lian B, Watanabe K, Taniguchi T, Bernevig B A and Yazdani A 2020 *Nature* **588** 610

[67] Saito Y, Ge J, Rademaker L, Watanabe K, Taniguchi T, Abanin D A and Young A F 2021 *Nat. Phys.* **17** 478

[68] Choi Y, Kim H, Peng Y, Thomson A, Lewandowski C, Polski R, Zhang Y, Arora H S, Watanabe K, Taniguchi T, Alicea J and Nadj-Perge S 2021 *Nature* **589** 536

[69] Wu S, Zhang Z, Watanabe K, Taniguchi T and Andrei E Y 2021 *Nat. Mater.* **20** 488

[70] Das I, Lu X, Herzog-Arbeitman J, Song Z D, Watanabe K, Taniguchi T, Bernevig B A and Efetov D K 2021 *Nat. Phys.* **17** 710

[71] Park J M, Cao Y, Watanabe K, Taniguchi T and Jarillo-Herrero P 2021 *Nature* **592** 43

[72] Pierce A T, Xie Y, Park J M, Khalaf E, Lee S H, Cao Y, Parker D E, Forrester P R, Chen S, Watanabe K, Taniguchi T, Vishwanath A, Jarillo-Herrero P and Yacoby A 2021 *Nat. Phys.* **17** 1210

[73] Klein D R, Xia L Q, MacNeill D, Watanabe K, Taniguchi T and Jarillo-Herrero P 2023 *Nat. Nanotechnol.* **18** 331

[74] Liang Y, Mao N, Dai Y, Kou L Z, Huang B B and Ma Y D 2021 *npj Comput. Mater.* **7** 172

[75] Wu F, Lovorn T, Tutuc E, Martin I and MacDonald A H 2019 *Phys. Rev. Lett.* **122** 086402

[76] Cai J, Anderson E, Wang C, Zhang X, Liu X, Holtzmann W, Zhang Y, Fan F, Taniguchi T, Watanabe K, Ran Y, Cao T, Fu L, Xiao D, Yao W and Xu X 2023 *Nature* **622** 63

[77] Zeng Y, Xia Z, Kang K, Zhu J, Knüppel P, Vaswani C, Watanabe K, Taniguchi T, Mak K F and Shan J 2023 *Nature* **622** 69

[78] Park H, Cai J, Anderson E, Zhang Y, Zhu J, Liu X, Wang C, Holtzmann W, Hu C, Liu Z, Taniguchi T, Watanabe K, Chu J H, Cao T, Fu L, Yao W, Chang C Z, Cobden D, Xiao D and Xu X 2023 *Nature* **622** 74

[79] Xu F, Sun Z, Jia T, Liu C, Xu C, Li C, Gu Y, Watanabe K, Taniguchi T, Tong B, Jia J, Shi Z, Jiang S, Zhang Y, Liu X and Li T 2023 *Phys. Rev. X* **13** 031037

[80] Foutty B A, Kometter C R, Devakul T, Reddy A P, Watanabe K, Taniguchi T, Fu L and Feldman B E 2024 *Science* **384** 343

[81] Zhang X W, Wang C, Liu X, Fan Y, Cao T and Xiao D 2024 *Nat. Commun.* **15** 4223

[82] Ahn C H, Bhattacharya A, Di Ventra M, Eckstein J N, Frisbie C D, Gershenson M E, Goldman A M, Inoue I H, Mannhart J, Millis A J, Morpurgo A F, Natelson D and Triscone J M 2006 *Rev. Mod. Phys.* **78** 1185

[83] Cao Y, Fatemi V, Demir A, Fang S, Tomarken S L, Luo J Y, Sanchez-Yamagishi J D, Watanabe K, Taniguchi T, Kaxiras E, Ashoori R C and Jarillo-Herrero P 2018 *Nature* **556** 80

[84] Cao Y, Fatemi V, Fang S, Watanabe K, Taniguchi T, Kaxiras E and Jarillo-Herrero P 2018 *Nature* **556** 43

[85] Rhodes D A, Jindal A, Yuan N F Q, Jung Y, Antony A, Wang H, Kim B, Chiu Y c, Taniguchi T, Watanabe K, Barmak K, Balicas L, Dean C R, Qian X, Fu L, Pasupathy A N and Hone J 2021 *Nano Lett.* **21** 2505

[86] Zhai B, Li B, Wen Y, Wu F and He J 2022 *Phys. Rev. B* **106** L140505

[87] Qin B, Ma C, Guo Q, Li X, Wei W, Ma C, Wang Q, Liu F, Zhao M, Xue G, Qi J, Wu M, Hong H, Du L, Zhao Q, Gao P, Wang X, Wang E, Zhang G, Liu C and Liu K 2024 *Science* **385** 99

[88] Xi X, Wang Z, Zhao W, Park J H, Law K T, Berger H, Forró L, Shan J and Mak K F 2016 *Nat. Phys.* **12** 139

[89] Xi X, Berger H, Forró L, Shan J and Mak K F 2016 *Phys. Rev. Lett.* **117** 106801

[90] Liu X, Pyatakov A P and Ren W 2020 *Phys. Rev. Lett.* **125** 247601

[91] Liu K, Ma X, Xu S, Li Y and Zhao M 2023 *npj Comput. Mater.* **9** 16

[92] Xun W, Wu C, Sun H, Zhang W, Wu Y Z and Li P 2024 *Nano Lett.* **24** 3541

[93] Zhang T, Liang Y, Xu X, Huang B, Dai Y and Ma Y 2021 *Phys. Rev. B* **103** 165420

[94] Garcia V, Bibes M, Bocher L, Valencia S, Kronast F, Crassous A, Moya X, Enouz-Vedrenne S, Gloter A, Imhoff D, Deranlot C, Mathur N D, Fusil S, Bouzehouane K and Barthélémy A 2010 *Science* **327** 1106

[95] Chen X F, Ding X K, Gou G Y and Zeng X C 2024 *Nano Lett.* **24** 3089

[96] Jafari H, Barts E, Przybysz P, Tenzin K, Kowalczyk P J, Dabrowski P and Sławińska J 2024 *Phys. Rev. Mater.* **8** 024005

[97] Meier D and Selbach S M 2022 *Nat. Rev. Mater.* **7** 157